

Landslides (2020) 17:2563–2576
 DOI 10.1007/s10346-020-01448-w
 Received: 13 January 2020
 Accepted: 28 May 2020
 Published online: 13 October 2020
 © Springer-Verlag GmbH Germany
 part of Springer Nature 2020

Gordon G. D. Zhou · Pamela Jessica Cacela Roque · Yunxu Xie · Dongri Song · Qiang Zou ·
 Huayong Chen

Numerical study on the evolution process of a geohazards chain resulting from the Yigong landslide

Abstract Geohazard chain processes in mountainous areas generally entail a landslide, followed by a dammed lake, a dam breach, and then outburst flooding. These chains have greater destructive power and a larger area of coverage than a single process, of which a representative event is the April 2000 Yigong landslide in Tibet, China. In this study, a two-part, numerical back-analysis of the entire chain process is carried out. Enhanced one-layer Savage-Hutter models, which incorporate a multiscale, empirical friction model (velocity-weakening) and appropriate erosion mechanics, are solved using a non-staggered central differencing scheme. A reasonable reproduction of the geohazard event chain was obtained. Results show that the use of the multiscale friction law is able to reproduce the dynamic process of the landslide with acceptable accuracy. In addition, the variation of soil shear resistance along the dam depth (against the water flow above) during the dam breach is considered in the study, in which the outburst flooding process is better modeled. The numerical results, validated by field measurements, provide reliable assessment and interpretation of the actual event.

Keywords Yigong landslide · Geohazard chain · Numerical simulation · Velocity-weakening friction · Dam breach

Introduction

Mountain-hazard chains are catastrophic chain reactions in which one or even several hazards are triggered by an antecedent disaster under certain conditions in a mountainous region. Typical disaster chains, including landslides, debris flow, landslide dam and dammed lake, and outburst flooding, are influenced by topography, geomorphology, amount of precipitation, and other factors (Pei et al. 2017). Since in a mountain-hazard chain, one sub-disaster is triggered after another, like a domino effect, the time scale at which the chain occurs greatly exceeds that of a single disaster and affects a greater amount of area. Particularly, earthquake-induced sub-disasters result in high casualties, structural damages, and significant financial losses (Han et al. 2019).

Among all of the mountain-hazard chains that occurred in China within the past century, the Yigong hazard chain, which initiated in southeast of Tibet (Fig. 1), has received the most global attention. This mountain-hazard chain event can be divided into two phases with four processes: the granular mass flow and dam formation in the first phase, and the landslide dam failure and resulting outburst flooding in the second phase.

A significant amount of work has already been devoted in studying the landsliding process up to the formation of the landslide dam (e.g., Xu et al. 2012; Zhou et al. 2013, 2015a, b; Delaney and Evans 2015; Liu and He 2018). Previous works have modeled the motion of the Yigong landslide using the Coulomb (Liu and He

2018) and Voellmy (Xu et al. 2012; Delaney and Evans 2015) friction laws which, despite being able to produce reasonable predictions, cannot fully account for high shearing rate and large internal deformations during the landslide motion nor are completely based on physical properties with an empirical turbulence coefficient (Zhou et al. 2013). Landslides can be alternatively viewed as dense granular flows wherein the rheology depends on its internal deformation and material properties expressed as a function of the so-called inertial number I (Jop et al. 2006). This constitutive law has been found to adequately define the rheology of laboratory-scale granular flows in different geometries (MiDi 2004). However, this rheological law is scale-limited and is only valid for dense laboratory (small scale) granular flows and thus cannot reproduce natural large-scale landslides (Lucas et al. 2014; Breard et al. 2019). Recently, Lucas et al. (2014) modified the I -dependent rheology to capture the weakening of the effective friction with velocity as observed in large and small flows on Earth and even on extra-terrestrial bodies (e.g., the moon and Iapetus). Therefore, this study adopts the empirical, multiscale friction law from Lucas et al. (2014) which relates the effective friction and the granular sliding velocity using a single set of parameters to estimate the dynamic behavior of granular mass flows.

The mass deposited by the landslide on the Yigong River formed a dam which eventually collapsed and resulted to massive flood which destroyed settlements downstream. The failure of the landslide dam was attributed to overtopping, a mechanism which is governed by the erodibility of dam materials (Chang and Zhang 2010; Zhang et al. 2019) and the hydraulics of the overflow flooding. The erosion on the surface of landslide dams is controlled by erosion rate E . Table 1 lists several ways to calculate E based on existing literatures. Roberts et al. (1998) proposed that E is exponentially related to the difference between the shear stress of the overflowing stream (τ) and the sediment erosion resistance (τ_c). The models of Hanson and Simon (2001) and Fraccarollo and Capart (2002), though derived differently, assume a linear dependence on $(\tau - \tau_c)$. On the other hand, Takahashi (1991) proposed an erosion rate that has both velocity and stress level dependency, based on the difference of the flow sediment concentration c and an equilibrium concentration c_e . Cao et al. (2004, 2011a, 2011b) adopted an empirical model with a non-dimensionalized shear stress based on the sediment transport in a tranquil river to separately define sediment erosion (E) and deposition rate (D) without any explicit dependence on the boundary traction.

The shear resistance τ_c is usually estimated from the soil properties (e.g., mean particle size, void ratio, density) of the landslide deposits (Smerdon and Beasley 1961; Vanoni 1964; Mehta 1988; Amos et al. 2004; Annandale 2006; Julian and Torres 2006; Chang and Zhang 2010). Table 2 lists some of the empirical

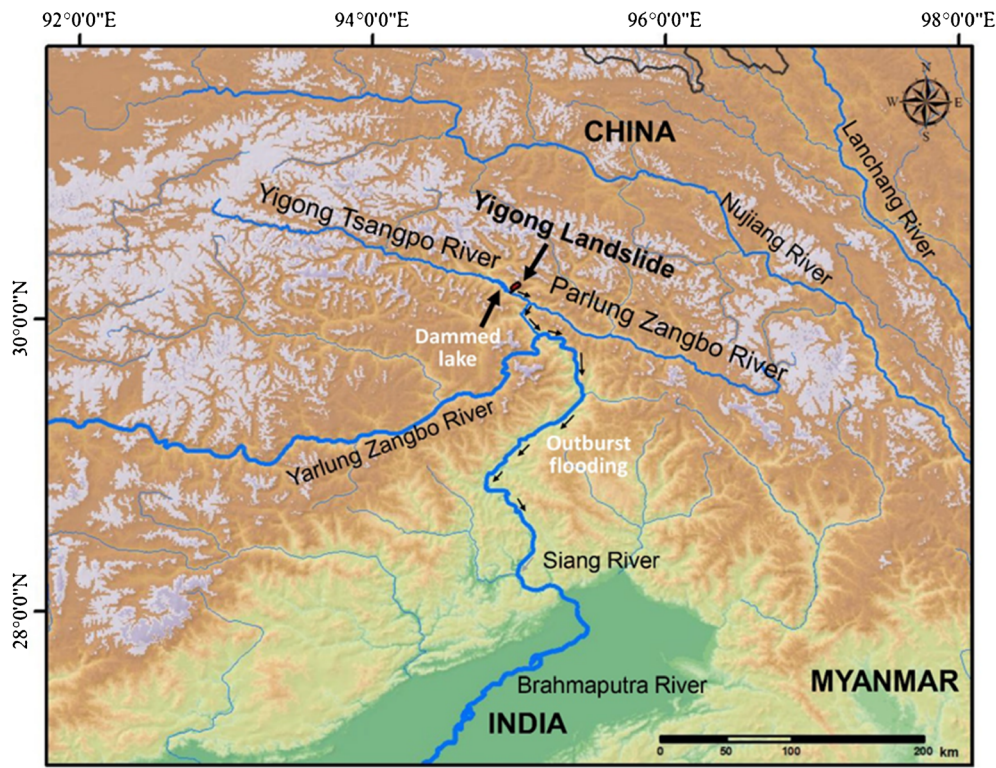


Fig. 1 Location of 2000 Yigong landslide and hazard chain

equations formulated to estimate the resistance of soil to erosion for dam failures. Shang et al. (2003) observed that the Yigong landslide dam was composed of cobble- and boulder-sized clasts, and some matrix-supported clasts with poor degree of sorting. Results of a field investigation conducted in April 2017 by the authors support these findings, noting a low fine content for the landslide dam. Thus, the shear resistance model of Annandale (2006) is identified to be most applicable for this study. Natural landslide dams are typically comprised of freshly deposited, heterogeneous, and unconsolidated or poorly consolidated materials (Chang and Zhang 2010), which yields a wider range of particle sizes (Costa and Schuster 1988; Casagli et al. 2003). Previous works disregard the drastic variation of erodibility along depth, which effectively influences the evolution of downstream flooding (cf. Chang and Zhang 2010). Delaney and Evans (2015) estimated the peak discharge using satellite imagery analysis, not taking into account the detailed failure process of the landslide dam. Liu and He (2018) adopted empirical dam failure mechanics established by Cao (1999) and Cao et al. (2011b) which assumes a uniform resistive shear stress for the landslide dam, and Turzewski et al. (2019) assumed an instantaneous dam failure at the breach to simulate the 2000 Yigong flood in GeoClaw. Therefore, this study adopts the depth-integrated erosion model (Fraccarollo and Capart 2002; Iverson 2012) which explicitly define τ exerted by the water flow and the τ_c from the deposited dam through a flow-bed interface relationship.

This paper presents an enhanced depth-averaged model, designed to separately define the evolution of geophysical flows or landslides, dam breaching, and flooding. The landslide model,

which includes the propagation and the deposition (river damming processes), is demonstrated using an up-to-date, multiscale friction law. As for the subsequent dam breach and flooding, both the dependence and the non-dependence of erodibility along the depth are considered in order to estimate the increasing breach process and resulting flood discharge. In order to verify the accuracy of the modeled results, the simulated height of the landslide dam and the flood traces were compared with those determined from field investigations and existing references. This study ultimately aims to provide reliable models for the dynamics of sub-disasters of natural hazard chains in order to further improve our understanding on their interactions and to help bolster natural hazard emergency management and mitigation capabilities.

Background of the geohazard chain induced by the Yigong landslide

At about 20:00 on 9 April 2000, a large-scale rock avalanche, with a total volume of about $9.1 \times 10^7 \text{ m}^3$ (Delaney and Evans 2015) traveled along the Zhamu Creek. The granular materials descended from an elevation of 3050 m and totally obstructed the downstream Yigong River. An irregularly shaped sediment deposit was formed with a height that ranged from 60 to 100 m and spread over an area of about 5 km^2 (Shang et al. 2003; Delaney and Evans 2015). The height of the landslide dam which formed from the said sediments ranged from 55.1 to 90 m (Yin 2000; Shang et al. 2003; Delaney and Evans 2015). After the dam formation, water in the Yigong Lake began to rapidly impound on its upstream face for 62 days before the catastrophic failure (Zhou 2000; Shang et al. 2003; Xu et al. 2012). The dammed lake enlarged from an initial area of 15 km^2 to that of 37.1 km^2 within 1 month

Table 1 Equations for calculating erosion rate (E)

Erosion model	Reference	Comment(s)
$E = a(\tau - \tau_c)^b$	Roberts et al. (1998)	a and b are dominated by sediment properties
$E = K_d(\tau - \tau_c)$	Hanson and Simon (2001)	Based on the erosive stress induced by flowing water
$E = \frac{(\tau - \tau_c)}{\bar{\rho} \bar{u}} = \frac{1}{\bar{\rho} \bar{u}} (\tau - \tau_c)$ (Adopted in this study)	Fraccarollo and Capart (2002); Iverson (2012)	Based on mass and momentum balance in a three-layer system
$E = \begin{cases} \alpha \frac{c_e - c}{c^* - c_e} \frac{h \bar{u}}{d} & \text{if } (c_e > c) \\ \beta \frac{c_e - c}{c^*} \frac{h \bar{u}}{d} & \text{otherwise} \end{cases}$	Takahashi (1991)	Based on the difference of solid concentration of the flow and an equilibrium concentration
$b=1$ $= \begin{cases} \alpha \left(\frac{c_e h \bar{u}}{(c^* - c_e) d} - \frac{c h \bar{u}}{(c^* - c_e) \tau_c} \right) & \text{if } (c_e > c) \\ \beta \left(\frac{c_e h \bar{u}}{\underline{c^* d}} - \frac{c h \bar{u}}{\underline{c^* d} \tau_c} \right) & \text{otherwise} \end{cases}$		
$E = \begin{cases} \eta u (\theta - \theta_c) d^{-0.2} h^{-1} & \text{if } (\theta \geq \theta_c) \\ 0 & \text{otherwise} \end{cases}$	Cao (2004)	Based on sediment transport
$= \begin{cases} \eta \left(\frac{\theta u}{d^{0.2} h} - \frac{\theta_c u}{d^{0.2} h} \right) & \text{if } (\theta \geq \theta_c) \\ 0 & \text{otherwise} \end{cases}$		

(Yin 2000) and the estimated impounded volume reached about $2 \times 10^9 \text{ m}^3$ before the dam breach (Shang et al. 2003; Zhu et al. 2003; Xu et al. 2012; Delaney and Evans 2015). The resulting flood destroyed agricultural land, downstream municipalities, and transportation systems and led to flooding of the Yarlung-Siang-Brahmaputra River system. Even at a distance of 17 km downstream of the landslide dam, a peak discharge of up to 120,000 m^3/s was reported (Shang et al. 2003; Xu et al. 2012; Delaney and Evans 2015).

Geographical and geological setting

The Yigong landslide occurred in the southern part of the Nyainqntanglha Range in southeast Tibet (Shang et al. 2003), an area surrounded by steep, high mountains with a narrow valley. The April 2000 Yigong landslide site was 26 km, 50 km, 95 km, and 50 km, away from the towns of Yigong, Lulang, and Bomi, and the Yarlu River, respectively (Xu et al. 2009; Zhou et al. 2015a). Zhamu Creek, which became the landslide drainage site, is approximately

9.7 km long with a total watershed area of 20.2 km^2 . The upper section of Zhamu Creek has an area covered with 2.2 km^2 permanent glacier and snow, with an elevation range of 3700–5520 m, a length of about 2.6 km, and side angles of about 40° . The landslide initiation site, shown as the boxed region in Fig. 2, has a maximum elevation of 5520 m (Shang et al. 2003; Xu et al. 2012) with a bare bedrock and slope region of 7.6 km^2 , and a total forested area of 10.4 km^2 (Lu et al. 1999). The horizontal distance from the source zone to Yigong river bed is 10.7 km with a mean longitudinal slope of 31° (Delaney and Evans 2015). During the 2000 Yigong landslide, the accumulative rainfalls during April 1–9 were measured to be over 50 mm (Liu and Lu 2000) and the total rainfall in April was about 100 mm, 50–90% more than the mean value from the same period in this area (Zhou 2000).

The rock masses at the slope surface have been exposed to extreme weathering conditions (Shang et al. 2003; Zhou et al. 2015a). These have layered cataclastic structures (Gu 1979) where joints and fractures are well developed. Tectonic movements and geomorphic evolutions have made the lithologic distribution at the

Table 2 Empirical equations for calculation of critical erosive shear stress of soil (τ_c)

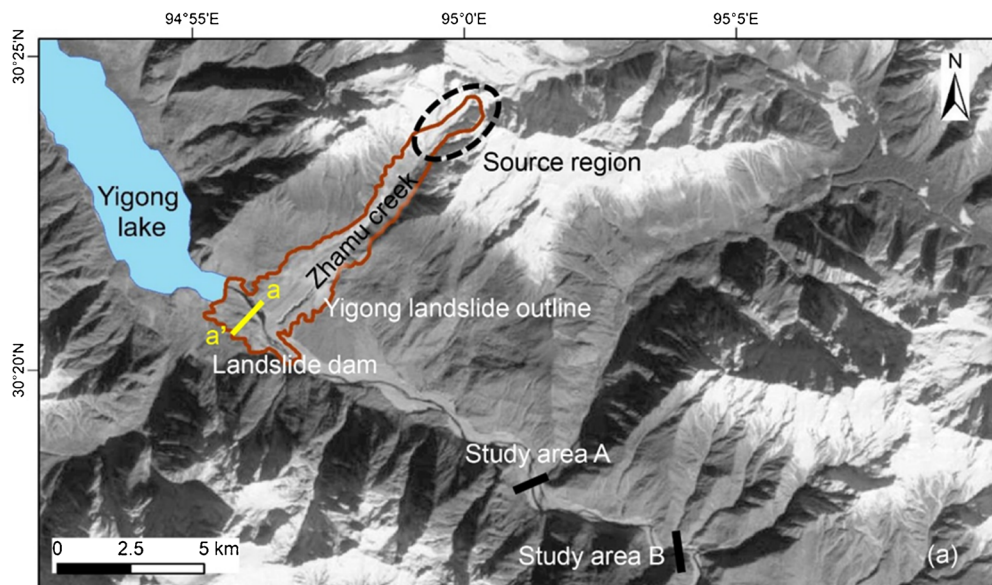
Empirical expression	Main parameters	References
$\tau_c = 3.54 \times 10^{-28.1d_{50}}$	d_{50} , mean particle size (m)	Smerdon and Beasley (1961)
$\tau_c = 0.16(PI)^{0.84}$	PI, plasticity index (%)	
$\tau_c = 0.493 \times 10^{0.0182P_c}$	P_c , percent of clay by weight (%)	
$\tau_c = 0.18 \tan \theta d_s (\gamma_s - \gamma)$	θ , repose angle of the sediment; d_s , median sieve size	Vanoni (1964)
$\tau_c = 0.0012 \rho_d^{1.2}$	ρ_d , dry density	Ockenden and Delo (1988)
$\tau_c = \xi(\rho_b - 1)$	ρ_b , bulk density of soil (kg/m ³); ξ , coefficient	Mehta (1988)
$\tau_c = 0.015(\rho_b - 1000)^{0.73}$	ρ_b , bulk density of soil (kg/m ³)	Mitchener and Torfs (1996)
$\tau_c = \tau_0 \left(\frac{H_p}{H_e} \right)^2$	τ_0 , maximum hydraulic shear stress; H_p , potential core length from the origin of the jet; H_e , distance from the jet nozzle to the equilibrium depth of scour	Hanson and Cook (1997)
$\tau_c = 5.44 \times 10^{-4} \rho_b - 0.28$	ρ_b , bulk density of soil (kg/m ³)	Amos et al. (2004)
$\tau_c = 0.1 + 0.1779P + 0.0028P^2 - 2.34 \times 10^{-5}P^3$	P , fines content (%)	Julian and Torres (2006)
$\tau_c = \frac{2}{3}gd(\rho_s - \rho_w)\tan\phi$ (adopted in this study)	ρ_w , mass density of water (kg/m ³), ρ_s , mass density of soil (kg/m ³); ϕ , friction angle	Annandale (2006)
$\tau_c = 6.8(PI)^{1.68}P^{-1.73}e^{-0.97}$	e , void ratio; PI, plasticity index (%)	Chang and Zhang (2010)

Yigong landslide area very complicated. The four main types of rocks in the research area are granite, marble, slate, and limestone, with different degrees of weathering and variability (Shang et al. 2003; Xu et al. 2012; Zhou et al. 2015a). At the upper segment of Zhamu Creek, the rock masses are mainly composed of granite and steep slate (Zhou et al. 2015a). Large volume of loose landslide deposits consisting of sandy silt, fragmented gravels, and other landslide debris materials also exist on the channel bed of the middle segment. At the lower segment, thick deposits of 1900-old

landslide or new debris flows are accumulated (Wang 2000; Delaney and Evans 2015). From the properties enumerated above, it is evident that the physical, geographical, and geological conditions of Zhamu Creek made it a perfect initial setting for a large-scale rock avalanche.

Field investigation

In this study, the Zhamu Creek and the adjacent Yigong River, are divided into three sections- the landslide dam by granular mass

**Fig. 2** Planform view of Zhamu Creek and Yigong landslide dam (with cross section a–a'), flood study areas A and B obtained from LANDSAT-7

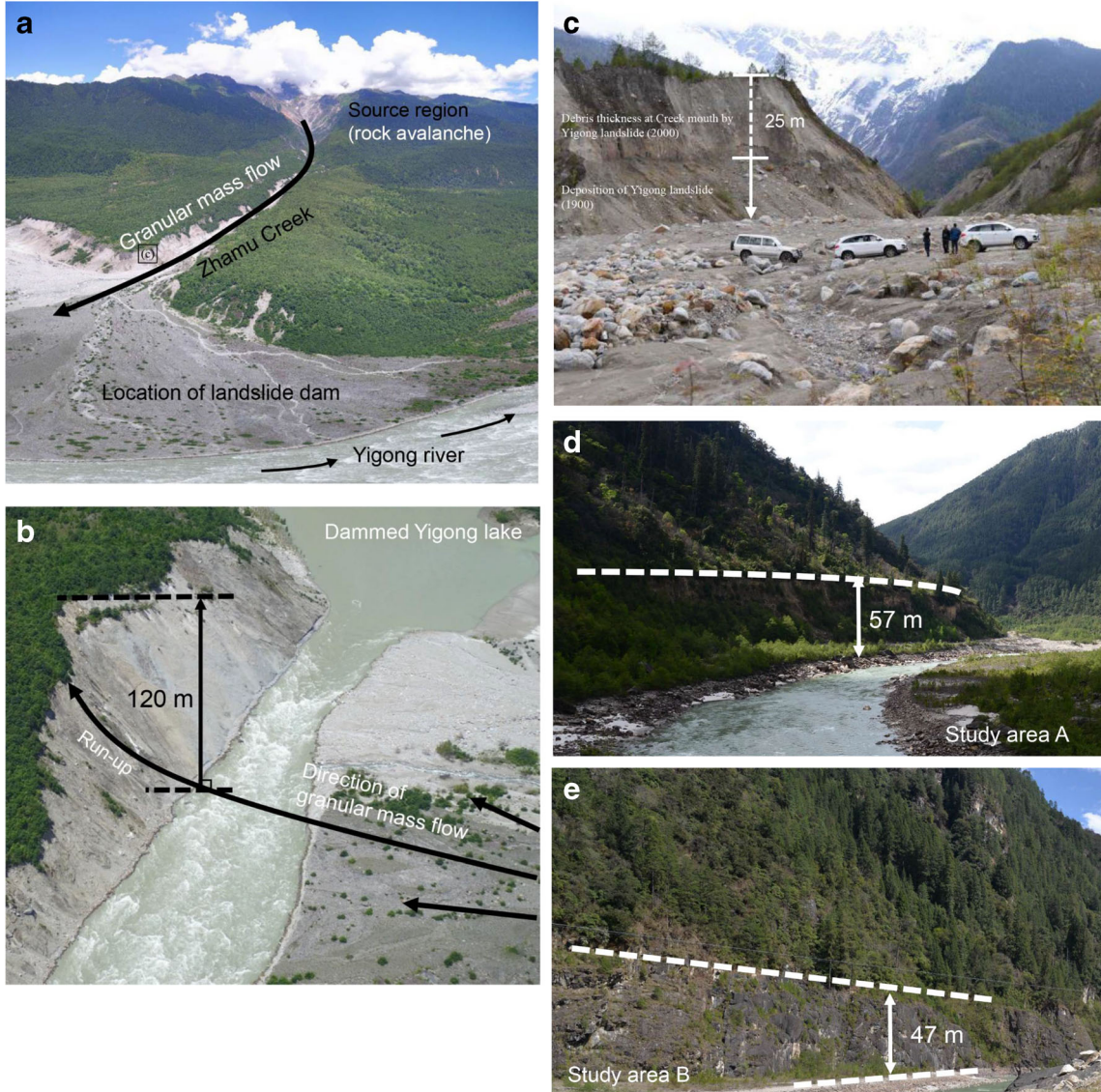


Fig. 3 Photographs of the entire Zhamu Creek, from the initiation zone to the deposition fan (a); the maximum reach height at and the far side bank (b); the debris deposited at the Creek mouth (c); d, e Detailed photographs of the dam and the study areas with the remaining flood traces of areas A and B from April 2017 field investigation

flow in 2000, and study areas A and B (Fig. 2). The distance from the deposition fan to study area A is 9.5 km while study areas A and B are 4.5 km apart. Figure 3a–e are obtained during the field investigation in April 2017. Figure 3a shows the initiation area and flowing path of the Yigong landslide. The deposition fan is observed to be longer on the downstream side, as reported previously by Shang et al. (2003). Using a handheld GPS and a laser range finder, an evident mud scratch of about 120 m on the far side of the bank (Fig. 3b) is measured. This mud scratch is attributed to the running up of the high-speed landslide from the side of origin to the opposite bank.

Flood surging downstream carries great kinetic energy, scours the vegetation and soil masses on the riverbank, and is later manifested as evident scratch lines. Such marks are similar to those observed at the riverbanks of the study areas A and B

(Fig. 3d, e). In study area A, the measured height of the scratch line is 57 m and 47 m at study area B. The heights of these scratch lines are used as reference values for the maximum inundated water levels during the outburst flooding.

Numerical study of granular mass flow and landslide dam formation

When highly mobilized granular mass moves downslope, the solid mass would eventually halt and pile up when it reaches the bottom valley and may cause a river blockage depending on the granular mass flow properties, river flow velocity, and river width (Fan et al. 2012). In this study, the granular mass ran up to the other bank of Yigong River causing total river blockage. The interaction of the granular mass flow and the river water when the solid mass plunged into the river is disregarded since the Yigong River flux is relatively small compared to that of the granular mass flows.

Granular mass flow model

For the first phase of this study, a single-phase model considering the dependency of friction on flow velocity is adopted to simulate the granular mass flow. Treating the granular flow system as a one-phase, isothermal mixture, the governing equations based on the conservation of mass and momentum are:

$$\partial_t \rho + \nabla \cdot (\rho \mathbf{u}) = 0 \quad (1)$$

$$\rho(\partial_t \mathbf{u} + (\mathbf{u} \cdot \nabla) \mathbf{u}) = -\nabla P + \nabla \cdot \boldsymbol{\tau} + \rho g \quad (2)$$

where ρ is flow density, g is gravitational acceleration, P is the fluid pressure, \mathbf{u} is the flow velocity vector, and $\boldsymbol{\tau}$ is the stress tensor. Since the characteristic length of granular body greatly exceeds the flow depth h for most granular mass flows, a fundamental assumption of the depth-average method (Savage and Hunter 1989), the following hyperbolic conservation laws derived from the conservation of mass and momentum equations are proposed:

$$\frac{\partial h_s}{\partial t} + \frac{\partial(h_s u_s)}{\partial x} + \frac{\partial(h_s v_s)}{\partial y} = 0 \quad (3)$$

$$\frac{\partial(h_s u_s)}{\partial t} + \frac{\partial(h_s u_s^2 + \frac{1}{2} k_{ap} g h_s^2)}{\partial x} + \frac{\partial(h_s u_s v_s)}{\partial y} = -g h_s \frac{\partial z_b}{\partial x} - f_{bx} \quad (4)$$

$$\frac{\partial(h_s v_s)}{\partial t} + \frac{\partial(h_s u_s v_s)}{\partial x} + \frac{\partial(h_s v_s^2 + \frac{1}{2} k_{ap} g h_s^2)}{\partial y} = -g h_s \frac{\partial z_b}{\partial y} - f_{by} \quad (5)$$

In vector form, they can be written as:

$$\frac{\partial \mathbf{U}}{\partial t} + \frac{\partial F(\mathbf{U})}{\partial x} + \frac{\partial G(\mathbf{U})}{\partial y} = 0 \quad (6)$$

$$\mathbf{U} = \begin{Bmatrix} h_s \\ h_s u_s \\ h_s v_s \end{Bmatrix}; F(\mathbf{U}) = \begin{Bmatrix} h_s u_s \\ h_s u_s^2 + \frac{1}{2} k_{ap} g h_s^2 \\ h_s u_s v_s \end{Bmatrix};$$

$$G(\mathbf{U}) = \begin{Bmatrix} h_s v_s \\ h_s u_s v_s \\ h_s v_s^2 + \frac{1}{2} k_{ap} g h_s^2 \end{Bmatrix}; \mathbf{S} = \begin{Bmatrix} 0 \\ -g h_s \frac{\partial z_b}{\partial x} - f_{bx} \\ -g h_s \frac{\partial z_b}{\partial y} - f_{by} \end{Bmatrix} \quad (7)$$

where h_s , $h_s u_s$, and $h_s v_s$ represent the granular mass flow thickness from the base to the free surface, and the discharge per unit width in the Cartesian x , y directions, respectively; u_s , and v_s are the depth-averaged velocity components in the x , y directions, respectively; k_{ap} is the lateral earth pressure coefficient; and $f_b = (f_{bx}, f_{by})$ represents the basal frictional resistance.

In order to solve these hyperbolic equations (Eqs. 3–5), a natural extension of Lax-Friedrich first-order scheme is adopted in this paper. This scheme avoids characteristic decomposition since there are no Riemann problems to be solved (Nessyahu and Tadmor 1990). Excessive Lax-Friedrich scheme viscosity is treated in such a way that it results in a second- or higher-order resolution Riemann-solver-free family of central differencing schemes (Sweby 1984; Jiang et al. 1999; Kurganov and Tadmor 2000). The discretization of both the physical and the numerical domains are identical, fixed, and determined by the spatial resolution of the

DEM; thus, each DEM pixel corresponds to one computational cell. To ensure numerical stability, the Courant-Friedrichs-Lowy (CFL) condition is satisfied in determining the allowable time step. More details on the scheme implementation are presented in the Appendix. Rock avalanches and granular mass flows are commonly composed of dry particles, in which pore fluid plays a negligible role and an exceptional runout is usually observed (Crosta et al. 2001). Thus, the basal friction is completely attributed to the solid part. Since results of the Coulomb and the Voellmy models are still quite unsatisfactory in simulating dynamic processes and characteristics of granular flows and the results from $\mu(I)$ rheology do not match natural observations (cf. Lucas et al. 2014), a universal, empirical velocity-weakening friction law (Eq. (8)) is adopted in this study:

$$\mu(U) = \left(\mu_w + \frac{(\mu_o - \mu_w)}{1 + \|U\|/U_w} \right) \quad (8)$$

where μ_w and μ_o are the dynamic and static friction coefficients, respectively, $\|U\|$ is the scalar amplitude of the velocity vector, and U_w is the characteristic velocity for the onset of weakening. Yamada et al. (2013, 2018) used the SHALTOP numerical model and seismic waveform inversion to estimate different sets of dynamic friction coefficients and velocity distributions during sliding for the velocity-dependent friction model $\mu(U)$ of four large-scale landslides. The approximated $\mu(U)$ parameters used in Yamada et al. (2018) are different from the values presented by Lucas et al. (2014), but nevertheless provided the best fit for the studied landslides.

The existing estimates on the volume of the initial source materials are mostly within the range 30–300 Mm³ (Shang et al. 2003; Xu et al. 2009, 2012; Delaney and Evans 2015; Zhou et al. 2015a). By comparing the pre- and post-event DEM data and previously published literatures, the volume of 9.1×10^7 m³ proposed by Delaney and Evans (2015) is adopted. The choice of entrainment formula will largely affect the calculated volume of the material surging down from the creek as it will affect the damming volume which will further influence the subsequent processes. However, for simplification, the effect of entrainment is not considered in this large-scale landslide numerical modeling though it may be significant in the upper and middle parts of the creek (Shang et al. 2003; Xu et al. 2009). The terrain data used is based on the 1970 pre-event digital topographic data which has a spatial resolution of 30 × 30 m.

Numerical results: Yigong landslide process

Figure 4 shows the simulated landslide event using $\mu(U)$ friction law as the granular mass surges down the Zhamu Creek. The initiation mechanics are neglected. The insets show the cross-sectional dam formation along the dam crest. After initiation, the flowing mass gains momentum as it moves downslope. At $t = 75$ s (Fig. 4a), the flow runs into a flatter region which is near the mouth of Zhamu Creek. Here, the velocity begins to decrease owing to a larger basal friction and smaller slope gradient. Meanwhile, the narrow creek no longer constrains the movement perpendicular to its direction which slumps the flow into a more natural and flatter shape. Between 120 and 140 s, in Fig. 4b, c, the flow rushes up to the right bank and flows back to the channel.

After a processing time of about 120 s, the flow runs into the junction point of Zhamu Creek and Yigong River. In this simulation, however, the interaction of water and granular flow is disregarded since the debris speed and volume are much greater than that of the water in river channel (Delaney and Evans 2015). At 128 s (Fig. 4b), the flow runs up to the opposite bank due to its great momentum. Mud scratches obtained from field investigations conducted on April 2017 showed that the flowing mass is capable of reaching a height of up to 120 m, reasonably close to the simulated value of 112 m. At about 138 s (Fig. 4c), the flowing body has descended and starts to move towards the bank on the side of the initiation site. After $t = 320$ s (Fig. 4e), the main body of the debris has stopped flowing and the debris has totally blocked the Yigong River with a maximum depth of 65 m, which falls within the range of heights estimated by Shang et al. (2003) and those simulated by Delaney and Evans (2015) (Figs. 4f and 5b). Similar to the observation of Wang (2008) during their field investigation, traces of debris mass along the mouth of Zhamu Creek are also visible in the simulation results (Figs. 4e and 5b).

By comparing the deposits obtained from different combinations of $\mu(U)$ parameters, it was determined that the best similarity with the actual event was achieved using $\mu_w = 0.18$, $\mu_o = 0.30$, and $U_w = 0.8$. The granular flow surged down from Zhamu Creek and had a runout distance of 8560 m. Simulated front and rear velocities of the flowing mass is shown with the 2D DAN-W results of Delaney and Evans (2015) in Fig. 5a. The maximum simulated velocity reached 138 m/s, similar to the velocity of 130 m/s calculated by Delaney and Evans (2015). Final deposit thickness reached 64.7 m at the Yigong River, comparable to the values from Shang et al. (2003) and Delaney and Evans (2015) (Figs. 4f and 5b). The results indicate the feasibility of the simplified three-dimensional, single-phase model, which adopts a velocity-dependent friction, in reproducing the 2000 Yigong rock avalanche. The total simulation time for the first phase is 320 s; nevertheless, after 280 s, the main body of the debris has stopped flowing except for some parts of the debris edge sloshing back and forth at areas with high slope gradient.

Numerical study of landslide dam failure and outburst flooding

During the overtopping failure process, the potential energy of the stored water gradually transforms into kinetic energy as water flows downslope. As the flow velocity increases, the soil erosion rate, which is closely correlated to flow velocity, should also increase (Cao 1999; Carrivick 2010; Zhou et al. 2015b; Walder 2016). The increasing erosion rate on the sloping bed would in turn intensify the breach evolution. As the declination of stored water level and enlargement of breach size continues, the stored water will eventually stop flowing and the final breach is formed.

Dam breaching and outburst flooding model

To simulate the dam failure and the subsequent flooding, a new physical law based, single-phase mode is proposed. The dam break is due to overtopping failure and the shape of the diversion channel induced by sediment transport will change depending on the amount of erosion (Chang and Zhang 2010; Zhou et al. 2012; Walder 2016; Liu and He 2018; Zhou et al. 2019). The mass and momentum conservation equations from Eqs. (3–5) are therefore re-written as follows for outburst

flood:

$$\frac{\partial h_w}{\partial t} + \frac{\partial(h_w u_w)}{\partial x} + \frac{\partial(h_w v_w)}{\partial y} = \frac{E}{1-p} \quad (9)$$

$$\begin{aligned} & \frac{\partial(h_w u_w)}{\partial t} + \frac{\partial(h_w u_w^2 + \frac{1}{2} k_{ap} g h_w^2)}{\partial x} + \frac{\partial(h_w u_w v_w)}{\partial y} \\ &= -g h_w \frac{\partial z_b}{\partial x} - f_{bx} - u_w \frac{E}{1-p} \end{aligned} \quad (10)$$

$$\begin{aligned} & \frac{\partial(h_w v_w)}{\partial t} + \frac{\partial(h_w u_w v_w)}{\partial x} + \frac{\partial(h_w v_w^2 + \frac{1}{2} k_{ap} g h_w^2)}{\partial y} \\ &= -g h_w \frac{\partial z_b}{\partial y} - f_{by} - v_w \frac{E}{1-p} \end{aligned} \quad (11)$$

where E is the bed erosion rate in the vertical direction along the bottom boundary; f_b is the total basal traction of the flood of which the Manning shear stress was adopted, i.e., $f_{bx} = \rho_w g n^2 u_w |u| h^{-\frac{1}{2}}$, $f_{by} = \rho_w g n^2 v_w |u| h^{-\frac{1}{2}}$; p is the porosity of landslide dam; and $u = (u_w, v_w)$ is the velocity vector while u_w, v_w are the velocity components of flood in x, y directions.

Analysis of mass and momentum exchange between the flowing layer and the underlying erodible sediment layer aids in the calculation of bed erosion and entrainment rate (Iverson 2012). A series of empirically derived equations for calculating erosion rates have been proposed in the literatures (see Table 1). In this study, the erosion rate is reciprocal to the flow velocity

$$E = \frac{\tau - \tau_c}{\bar{\rho} \bar{u}} \quad (12)$$

$$\tau = f_b = \rho_w g n^2 u^2 h^{-\frac{1}{3}} \quad (13)$$

where ρ_w is the flood density, assumed to be constant at 1000 kg/m³ and τ_c is the critical erosive shear resistance of the landslide dam. The numerator in Eq. (12) represents an effective boundary shear stress, which is the difference between the basal shear traction (τ) by the flowing body and the boundary shear resistance (τ_c) by the erodible bed, and τ is the total basal traction of the impounded water, in which Manning's shear stress was adopted (Table 3). According to the theory of water flow in the open channels, mechanics of sediment transport, and Manning equation (Manning 1891), the Manning roughness parameter n takes into account the sediment flow property and channel roughness. The channel morphology of the Yigong River is rugged in which several large particles are randomly distributed as confirmed by field observation (Fig. 3) and Google Earth imagery (cf. Turzewski et al. 2019). Meanwhile, previous outburst flood studies (e.g., Chen and Peng 2006; Denlinger and DRH 2009; Bohorquez et al. 2015; Liu and He 2018; Turzewski et al. 2019) also show that $n = 0.05$ can be used for mega flood simulations from which reasonable predictions can be made. Therefore, the value of Manning's roughness parameter $n = 0.05$ is chosen in this paper.

A constant influx from the upper reach is applied to simulate the filling of the dammed lake. Eventually, the impounded water level reaches the highest dam crest elevation and starts to spill out from the dam crest, initiating the overtopping failure.

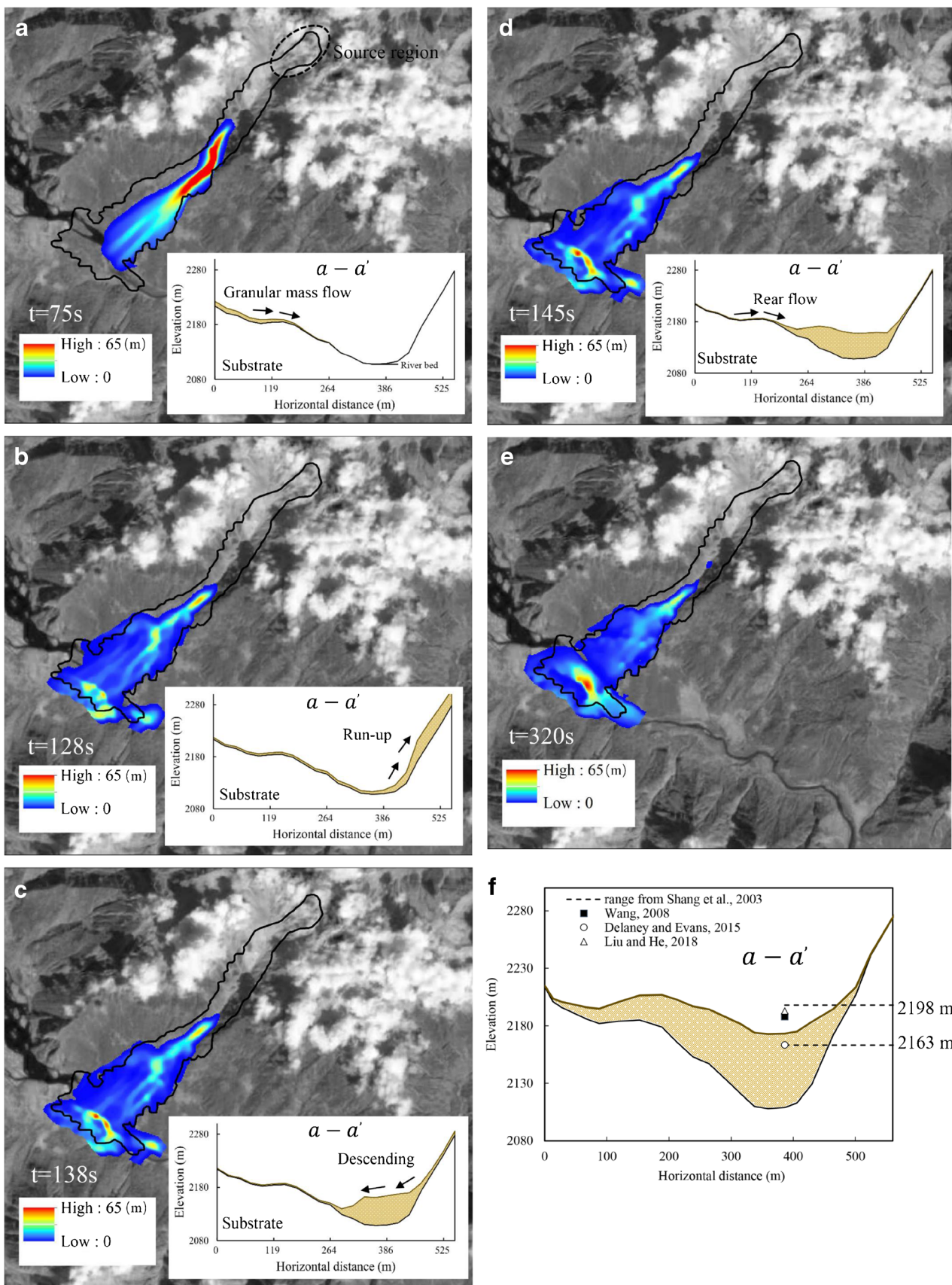


Fig. 4 a–e Best-fit elevation map outputs from the simulation at different time steps, with corresponding river cross section $a-a'$ damming process (inset). f Final dam formed at $t = 320\text{ s}$. The friction model parameters used are as follows: $\mu_w = 0.18$, $\mu_o = 0.30$, and $U_w = 0.8$

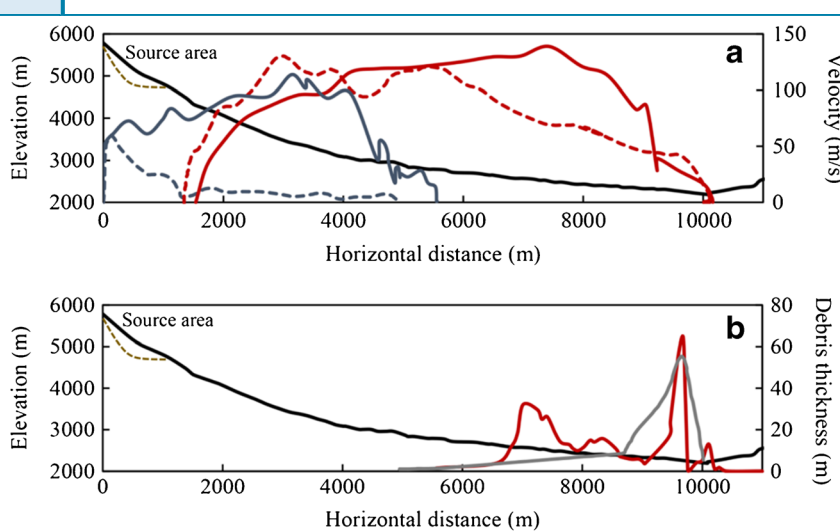


Fig. 5 a Simulated front (red) and back (blue) velocity profiles (dashed = Delaney and Evans (2015), solid = this study). Delaney and Evans (2015) rock avalanche topographic profile shown in black, with estimated source region (dashed brown). b Simulated landslide deposit profile (red) using the following friction parameters: $\mu_w = 0.18$, $\mu_o = 0.30$, and $U_w = 0.8$. Gray profile is from Delaney and Evans (2015) adopting empirical Voellmy rheology

Consequently, the erodible landslide dam material can greatly influence the crest breach evolution. Higher soil erodibility will lead to a faster and larger breach, resulting in a higher discharge value while lower soil erodibility results to milder soil and flood responses. For this reason, two distinct cases which consider the shear resistance of the landslide dam are used in this paper to compare the soil response after dam break. In model T1, the erodibility along depth is disregarded due to the assumption that the consolidation conditions are poor. The critical erosive shear resistance is calculated as (cf. Annandale 2006):

$$\tau_c = \frac{2}{3} g d_{50} (\rho_s - \rho_w) \tan \phi \quad (14)$$

where ρ_s and ρ_w are the density of soil and water, respectively; d_{50} is mean particle size; and ϕ is the internal friction angle of soil.

Shear resistance of the soil (τ_c) is dependent on the normal stress it experiences, which increases with depth. The field study of the Xiaogangjian, Tangjiashan, and Baige landslide dams confirm that shear resistance (τ_c) increases along dam depth (Chang and Zhang 2010; Chang et al. 2011; Zhang et al. 2019; Fig. 6). To simplify the depth dependence of τ_c , the erodibility evolution is divided into two parts. Soils at depths shallower than 10 m, primarily composed of large-size boulders with sands and clays, have low degree of consolidation due to the relatively low normal stress. Accordingly, for the numerical simulation, a constant shear resistance along the depth is calculated from Eq. (14) for soil at top layers. For the soils at depths greater than 10 m from the surface,

which are exposed to greater normal stresses, the field measurement illustrates that the shear resistance increases with dam depth (Fig. 6). The field measurement values are used as reference in which the average slope obtained is applied for determining the shear resistance at depths greater than 10 m of the Yigong landslide dam. With this, a new basal shear resistance relation (model T2) is proposed, taking into account the significant landslide dam erodibility variation along the depth D , consistent with the field observations from the Xiaogangjian, Tangjiashan, and Baige landslide dams (Chang and Zhang 2010; Zhang et al. 2019).

Numerical results: dam break and flooding

To simplify the lake filling process, a constant flux of $8 \times 10^6 \text{ m}^3/\text{s}$ from the upstream of the lake is applied until the water level reaches the dam crest, signaling the initiation of overtopping. The maximum volume of water for the dammed lake is $2 \times 10^9 \text{ m}^3$ (Delaney and Evans 2015). After the breach begins to form, the overtopping flow interacts with the erodible dam by applying traction on the poorly consolidated soil particles. The erosion along the depth and lateral directions show little difference at the early parts of the erosion process ($t = 0\text{--}200 \text{ s}$) as shown in Fig. 7a, b since, as shown in Fig. 6, the shear resistance of model's T1 and T2 are equal to each other at shallow layers ($<10\text{m}$). T1 is equal throughout the depth while T2 increases exponentially. As the water velocity increases, the soil erosion rate increases as does the breach expansion. The erosion rate of the dam with T1 increases after 200 s, and the peak discharge is recorded at around 300 s. After which, the discharge decreases as the water level of dammed lake decreases and the dam stabilizes. The erosion rate of

Table 3 τ_c models used for calculation of E

Erosion law	Model	Critical shear stress (kPa)
$E = \frac{\tau - \tau_c}{\rho u}$	T1	$\tau_c = 50$
	T2	$\tau_c = \begin{cases} 50 & (D < 10\text{m}) \\ 50 + 10(\frac{D+15.6}{15.2}) & (D \geq 10\text{m}) \end{cases}$

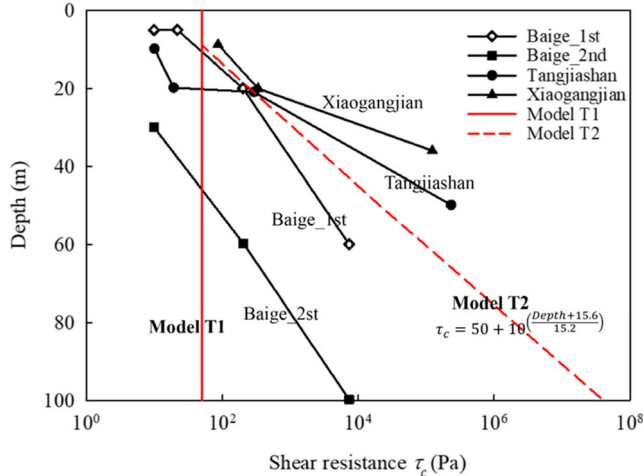


Fig. 6 Erosive shear resistance (τ_c) variation along depth

the dam using the T2 model however does not immediately increase after 200 s since the shear resistance increases with the depth making it harder to entrain the particles of the dam. That is why, unlike T1 in which the dam is fully eroded after 670 s, only 54% of the dam along the crest is eroded using T2. An analogous

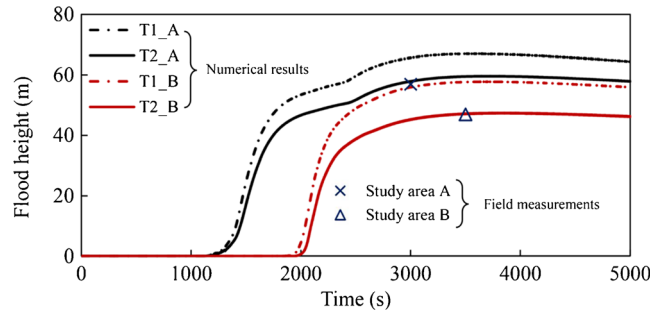


Fig. 8 Outflow hydrograph at study areas A (black) and B (red). T1 (dashed line) assumes constant erodibility while T2 (solid line) considers erodibility along depth. Maximum flood heights based on April 2017 field investigation are 57 m for study area A and 47 m for study area B

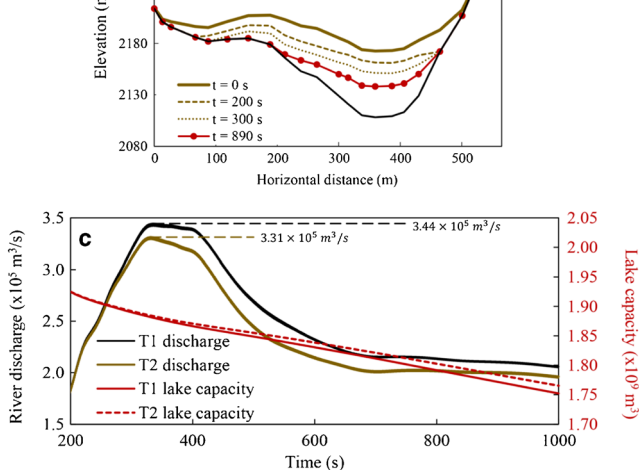
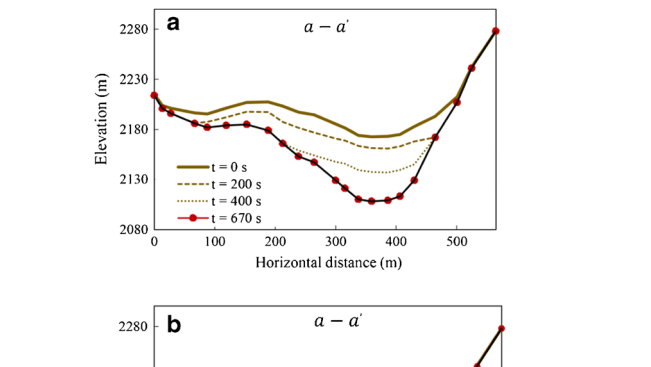


Fig. 7 Evolution of dam crest breach along cross section a-a' of a uniform τ_c (model T1) and b depth-dependent τ_c (model T2). c Simulated results of breach flow rate and lake water level changes

breaching flow rate pattern due to the breach initiation and development phases has also been observed by Zhang et al. (2019) at the two Baige landslide dams which failed due to overtopping. As expected, lower peak discharge is calculated for T2 (Fig. 7c). Average discharge can be calculated by dividing the maximum dammed lake capacity with the outburst duration. The resulting average discharge for T1 and T2 are $1.93 \times 10^5 \text{ m}^3/\text{s}$ and $1.70 \times 10^5 \text{ m}^3/\text{s}$, respectively. They are approximately equal to $1.86 \times 10^5 \text{ m}^3/\text{s}$ as calculated by Liu and He (2018), in which a coupled model for the water flow and sediment transport is used while adopting the entrainment rate proposed by Cao (1999). Moreover, Zhu et al. (2003) also have estimated an average discharge of $1.39 \times 10^5 \text{ m}^3/\text{s}$ based on field observation, which is smaller than the simulated values using T1, T2, and that of Liu and He (2018).

It is noted, however, that the maximum breach and downstream discharges for the 2000 Yigong event are not well constrained (Delaney and Evans 2015). Delaney and Evans (2015) estimated a peak breach discharge of $6.1 \times 10^4 \text{ m}^3/\text{s}$. Liu and He (2018) simulated a maximum breach discharge of about $3.5 \times 10^5 \text{ m}^3/\text{s}$, and Turzewski et al. (2019) reported a peak breach discharge of $1.73 \times 10^5 \text{ m}^3/\text{s}$ for $n = 0.4$. Our calculated peak discharges reached $3.44 \times 10^5 \text{ m}^3/\text{s}$ and $3.31 \times 10^5 \text{ m}^3/\text{s}$ for T1 and T2, respectively. These values are closest to the simulated values of Liu and He (2018), which also considered the influence of dam breach evolution in breach discharge. The huge differences from the estimated peak discharges by Delaney and Evans (2015) and Turzewski et al. (2019) are attributed to the fact that both studies disregarded the effects of the dam failure mechanism on the breach discharge. Delaney and Evans (2015) used an empirical estimate based on satellite imagery analysis of the total lake size while Turzewski et al. (2019) assumed instantaneous dam failure at the start of the simulation. Furthermore, the breach discharge profiles have also been found to vary depending on the Manning's roughness parameter (n) used (Turzewski et al. 2019), but is outside the scope of this study.

As the outburst flood moves downstream, it carries a great amount of kinetic energy which may result to the scouring of the riverbanks. Higher breaching flow rate indicates greater risk to the downstream areas. Figure 8 shows the simulated flood levels at downstream study areas A and B of models T1 and T2. After a processing time of 1100 s, the flood water reaches the study area A

while the flood passes area B at around 2000 s. Maximum flood levels at Study areas A and B, calculated using T₁, are 67 m and 58 m, respectively. Using T₂, a 60-m flood height is calculated for study area A and 47 m for study area B. To evaluate the simulated maximum inundation values for the two study areas, these were compared to the mud scratches measured from the April 2017 field investigation. T₁, which considered a uniform shear bed resistance along the dam depths, appears to have overestimated the downstream flood levels. T₂, which considers the variability of the landslide dam erosion along the depth that closely resembles that of the natural observations (Chang and Zhang 2010; Zhang et al. 2019), best fits the measured maximum water level for both study areas signifying the applicability of the modified τ_c model in describing the dam break process. We note however that there is still uncertainty in the flood heights simulated attributed to the simplifications of the numerical model, such as assumption of a single-phase flowing material, and zero entrainment for flood paths without dam deposits from the first phase (section 3).

Conclusions

Through a comprehensive numerical analysis, it is demonstrated that the whole process of the 2000 Yigong geohazard chain can be divided into two stages—the dynamic granular mass flow and the lake impounding, dam breach, and outburst flooding, with each stage simulated using a simplified, single phase, depth-averaged, numerical model (Table 4). Data from literatures and field measurement are used to verify the simulated results. The key conclusions that can be drawn are as follows:

1. The numerical study adequately simulates the rapid granular mass flow process: simplified initiation and propagation processes using a velocity-weakening friction law. The computed results are verified by both values from literatures and field measurement, indicating the feasibility of the simplified numerical model, which adopts a velocity-dependent friction law, in simulating the large-scale Yigong landslide and the resulting landslide dam formation.
2. The overtopping failure process of the landslide dam and the outburst flooding is numerically modeled. The consistent results between the field measurement (flood inundation at two different locations) and the numerical simulation illustrate the accuracy of the proposed erosion model for the dam breach. This model considers the variable shear resistance (τ_c) against the water flow along dam depth, which is in accordance with field studies.

Modeling geohazard chain remains a challenging endeavor. In order to simplify the process, this study used depth-averaged, single-phase conservation equations. The initiation mechanism and the channel erosion process during the granular mass flow are not within the scope of this study. More accurate simulation results may be obtained by taking into account the dynamics of multiple-phase flows before and after the dam breach, downstream river bed entrainment among others.

Acknowledgements

The authors acknowledge financial support from the National Natural Science Foundation of China (grant nos. 41941017,

41731283), Key Research Program of Frontier Sciences, CAS (grant no. QYZDB-SSW-DQC010), and the Sichuan Science and Technology Planning Program (grant no. 19YYJC0660).

Notations The following symbols are used in this paper:

a, b	coefficients
c	solid concentration of the flow
c^*	static bed solid concentration
c_e	equilibrium concentration
d, d_s, d_{50}	sediment particle diameter
E	erosion rate
e	void ratio
F, G, U, S	vectors defined in Eq. (7).
f_b	total basal traction
f_{bx}	x-component of the basal traction
f_{by}	y-component of the basal traction
g	gravitational acceleration
H_e	distance from the jet nozzle to the equilibrium depth of scour
H_p	potential core length from the origin of the jet
h, h_w	flow height
h_s	granular mass flow height
k_{ap}	lateral earth pressure coefficient
K_d	coefficient of erodibility
n	Manning's coefficient
P	fluid pressure
p	porosity of landslide dam
P_c	clay content by weight
PI	plasticity index
t	time
U	sliding velocity
u	depth- averaged velocity vector
u_s, u_w	x-component of depth- averaged velocity
U_w	characteristic velocity for the onset of weakening
v_s, v_w	y-component of depth-averaged velocity
z_b	bed elevation
α, β, η, ξ	empirical erosion coefficients
γ	specific weight of sediment fluid
γ_s	specific weight of sediment grain
θ	Shields parameter
θ_c	critical Shields parameter for initiation of sediment movement
μ	friction coefficient
μ_o	static friction coefficient
μ_w	dynamic friction coefficient
ρ, ρ_w	flow density
$\bar{\rho}, \rho_b$	bulk density
ρ_s	granular material density
τ	shear stress by the overflow streams
τ_o	maximum hydraulic shear stress
τ_c	critical erosive shear resistance of the dam
ϕ	internal friction angle

Appendix

Central differencing schemes are often used to solve nonlinear dynamic equations since they are not linked to the specific eigenstructure of the problem and can thus be implemented in a more straightforward way. The first-order Lax-Friedrichs scheme is the forerunner for such central schemes. The central Nessyahu-

Table 4 Parameters used in numerical simulations including granular mass flow, landslide dam overtopping failure, and outburst flooding

Scope	Parameter	Definition	Value
Granular mass flow	μ_0	Static friction coefficient	0.3
	μ_w	Dynamic friction coefficient	0.18
	U_w	Characteristic velocity for the onset of weakening	0.8
	ρ_d	Granular material density (kg/m^3)	2650
Landslide dam	p	Porosity of landslide dam	0.4
	d_{50}	Mean particle size (m)	0.01
	$\tan\phi$	Tangent of internal friction angle	0.5
Outburst flood	ρ_w	Flood density (kg/m^3)	1000
	n	Manning coefficient	0.05

Tadmor (NT) scheme offers higher resolution while retaining the simplicity of the Riemann-solver-free approach. Godunov's original scheme is also the forerunner of all upwind schemes. Though its higher-order and multi-dimensional generalizations were constructed, it requires characteristic information along the discontinuous interfaces of these spatial cells using approximate Riemann solvers, dimensional splitting, etc. which greatly complicates the upwind methods.

In this section, we first briefly introduce the high-resolution scheme on staggered grids over regular square grids- the NT scheme (Nessyahu and Tadmor 1990), which is regarded as a natural extension of the first-order LxF scheme. The cells in the NT scheme alternate every adjacent time step Δt . The importance of staggering is due to the fact that cell interfaces are stable in neighborhoods around the smooth regular mid-cells of the previous time step (Jiang et al. 1999). The two-dimensional system of conservation laws Equations without source terms are proposed:

$$\frac{\partial \mathbf{U}}{\partial t} + \frac{\partial f(\mathbf{U})}{\partial x} + \frac{\partial g(\mathbf{U})}{\partial y} = 0 \quad (15)$$

Lax and Friedrich introduced the first-order stable central scheme, the general Lax-Friedrich scheme:

$$\overline{U}_{i+\frac{1}{2},j+\frac{1}{2}}^{n+1} = \overline{U}_{i,j}^n - \lambda \left(f\left(\overline{U}_{i+1,j}^n\right) - f\left(\overline{U}_{i,j}^n\right) \right) - \eta \left(g\left(\overline{U}_{i,j+1}^n\right) - g\left(\overline{U}_{i,j}^n\right) \right) \quad (16)$$

Here, $\lambda = \frac{\Delta t}{\Delta x}$ and $\eta = \frac{\Delta t}{\Delta y}$ denote the mesh ratios of fixed size.

As a first step, we use the piecewise constant solution of the form $\sum \overline{U}_{ij}^n \chi_{ij}(x, y)$, in which \overline{U}_{ij}^n is the approximate cell average at t^n , associated with the cell $C_{ij} = \{(x-x_i) \leq \frac{\Delta x}{2}, (y-y_j) \leq \frac{\Delta y}{2}\}$ centered at (x_i, y_j) , $x_i = \Delta x \cdot i, y_j = \Delta y \cdot j$. The function $\chi_{ij}(x, y)$ is the characteristic function of the cell C_{ij} , i.e., $\chi_{ij}(x, y) = 1_{C_{ij}}$.

We construct a piecewise-linear approximation of the form:

$$U(x, y, t^n) = \sum \left(\overline{U}_{ij} + \dot{U}_{ij} \left(\frac{x-x_i}{\Delta x} \right) + \dot{U}_{ij} \left(\frac{y-y_j}{\Delta y} \right) \right) \chi_{ij}(x, y) \quad (17)$$

where \dot{U}_{ij} and \dot{U}_{ij} are discrete slopes in the x, y direction. To guarantee second-order accuracy, \dot{U}_{ij} and \dot{U}_{ij} should satisfy:

$$\dot{U}_{ij} \sim \Delta x \cdot U_x(x_i, y_j, t^n) + o(\Delta x)^2 \quad (18)$$

$$\dot{U}_{ij} \sim \Delta y \cdot U_y(x_i, y_j, t^n) + o(\Delta y)^2 \quad (19)$$

The second step is to replace the exact solution at next time step t^{n+1} by its averages over staggered cells: $C_{i+\frac{1}{2},j+\frac{1}{2}} = I_{i+\frac{1}{2}} \times J_{j+\frac{1}{2}}, C_{i+\frac{1}{2},j+\frac{1}{2}} = \{|x-x_{i+\frac{1}{2}}| \leq \frac{\Delta x}{2}, |y-y_{j+\frac{1}{2}}| \leq \frac{\Delta y}{2}\}$, integrate the equation over the staggered control volume $C_{i+\frac{1}{2},j+\frac{1}{2}} \times [t^n, t^{n+1}]$ yield:

$$\overline{U}_{i+\frac{1}{2},j+\frac{1}{2}}(t^{n+1}) = \overline{U}_{i+\frac{1}{2},j+\frac{1}{2}}(t^n) - \lambda \left(\frac{1}{|\Delta t|} \frac{1}{|J_{j+\frac{1}{2}}|} \int_{t^n}^{t^{n+1}} \int_{I_{i+\frac{1}{2}}} \left(f(U(x_{i+1}, y, t)) - f(U(x_i, y, t)) \right) dy dt \right) - \eta \quad (20)$$

$$\left(\frac{1}{|\Delta t|} \frac{1}{|I_{i+\frac{1}{2}}|} \int_{t^n}^{t^{n+1}} \int_{J_{j+\frac{1}{2}}} \left(g(U(x, y_{j+1}, t)) - g(U(x, y_j, t)) \right) dx dt \right)$$

Here $\overline{U}_{i+\frac{1}{2},j+\frac{1}{2}}(t^{n+1}) = \frac{1}{|C_{i+\frac{1}{2},j+\frac{1}{2}}|} \iint_{C_{i+\frac{1}{2},j+\frac{1}{2}}} U(x, y, t^{n+1}) dx dy$, $\overline{U}_{i+\frac{1}{2},j+\frac{1}{2}}(t^n) = \frac{1}{|C_{i+\frac{1}{2},j+\frac{1}{2}}|} \iint_{C_{i+\frac{1}{2},j+\frac{1}{2}}} U(x, y, t^n) dx dy$ denote the cell averages over staggered grids.

The next step is to evaluate the staggered grid averages $\overline{U}_{i+\frac{1}{2},j+\frac{1}{2}}(t^n)$ in Eq. 20:

$$\overline{U}_{i+\frac{1}{2},j+\frac{1}{2}}(t^n) = \frac{1}{|C_{i+\frac{1}{2},j+\frac{1}{2}}|} \iint_{C_{i+\frac{1}{2},j+\frac{1}{2}}} U(x, y, t^n) dx dy = \sum_{i=1}^4 \frac{1}{|A_i|} \iint_{A_i} U(x, y, t^n) dx dy \quad (21)$$

Here, the staggered cell $C_{i+\frac{1}{2},j+\frac{1}{2}}$ can be separated into $\sum_{i=1}^4 A_i$, where A_1, A_2, A_3 , and A_4 represent the cell: $\{(x_i, x_{i+\frac{1}{2}}) \times (y_{j+\frac{1}{2}}, y_{j+1})\}$, $\{(x_{i+\frac{1}{2}}, x_{i+1}) \times (y_{j+\frac{1}{2}}, y_{j+1})\}$, $\{(x_{i+\frac{1}{2}}, x_{i+1}) \times (y_j, y_{j+\frac{1}{2}})\}$, and $\{(x_i, x_{i+\frac{1}{2}}) \times (y_j, y_{j+\frac{1}{2}})\}$, respectively.

Using the integration over A_1 for example:

$$\begin{aligned} & \frac{1}{|A_1|} \iint_{A_1} U(x, y, t^n) dx dy \\ &= \frac{1}{|\Delta x|} \frac{1}{|\Delta y|} \int_{x_i}^{x_{i+\frac{1}{2}}} \int_{y_{j+\frac{1}{2}}}^{y_{j+1}} \left(\overline{U}_{ij} + U_{ij} \left(\frac{x-x_i}{\Delta x} \right) + U_{ij} \left(\frac{y-y_j}{\Delta y} \right) \right) dx dy \quad (22) \end{aligned}$$

The other three cell averages can be treated the same way. By adding the four integrals, the value of the staggered average

$\bar{U}_{i+\frac{1}{2},j+\frac{1}{2}}(t^n)$ can be expressed as:

$$\begin{aligned}\bar{U}_{i+\frac{1}{2},j+\frac{1}{2}}(t^n) &= \frac{1}{4} \left(\bar{U}_{i,j}^n + \bar{U}_{i+1,j}^n + \bar{U}_{i,j+1}^n + \bar{U}_{i+1,j+1}^n \right) \\ &\quad + \frac{1}{16} ((\dot{U}_{i,j} + \dot{U}_{i,j+1} - \dot{U}_{i+1,j} - \dot{U}_{i+1,j+1}) \\ &\quad + (\dot{U}_{i,j} + \dot{U}_{i+1,j} - \dot{U}_{i,j+1} - \dot{U}_{i+1,j+1}))\end{aligned}\quad (23)$$

The next step is to approximate the fluxes in equation:

$$\begin{aligned}&\frac{1}{|\Delta t|} \frac{1}{|J_{j+\frac{1}{2}}|} \int_{t^n}^{t^{n+\frac{1}{2}}} \int_{J_{j+\frac{1}{2}}} \left(f(U(x_{i+1}, y, t)) - f(U(x_i, y, t)) \right) dy dt \\ &\approx \frac{1}{|J_{j+\frac{1}{2}}|} \int_{J_{j+\frac{1}{2}}} (f(U(x_{i+1}, y, t^{n+\frac{1}{2}})) - f(U(x_i, y, t^{n+\frac{1}{2}}))) dy \\ &\approx \frac{1}{2} \{ (f(U_{i+1,j}^{n+\frac{1}{2}}) + f(U_{i+1,j+1}^{n+\frac{1}{2}})) - (f(U_{i,j}^{n+\frac{1}{2}}) + f(U_{i,j+1}^{n+\frac{1}{2}})) \}\end{aligned}$$

$$\bar{U}_{i+\frac{1}{2},j+\frac{1}{2}}(t^n) = \frac{1}{4} \left(\bar{U}_{i,j}^n + \bar{U}_{i+1,j}^n + \bar{U}_{i,j+1}^n + \bar{U}_{i+1,j+1}^n \right) + \frac{1}{16} ((\dot{U}_{i,j} + \dot{U}_{i,j+1} - \dot{U}_{i+1,j} - \dot{U}_{i+1,j+1}) + (\dot{U}_{i,j} + \dot{U}_{i+1,j} - \dot{U}_{i,j+1} - \dot{U}_{i+1,j+1})) - \frac{\lambda}{2} \{ (f(U_{i+1,j}^{n+\frac{1}{2}}) - f(U_{i,j}^{n+\frac{1}{2}})) + (f(U_{i+1,j+1}^{n+\frac{1}{2}}) - f(U_{i,j+1}^{n+\frac{1}{2}})) \}\quad (25)$$

$$-\frac{\eta}{2} \{ (g(U_{i,j+1}^{n+\frac{1}{2}}) - g(U_{i,j}^{n+\frac{1}{2}})) + (g(U_{i+1,j+1}^{n+\frac{1}{2}}) - f(U_{i+1,j}^{n+\frac{1}{2}})) \}\quad (25)$$

The values $f(U_{i,j}^{n+\frac{1}{2}})$ can be evaluated by Taylor's expansion and conservation law Eq. 15:

$$U_{i,j}^{n+\frac{1}{2}} = \bar{U}_{i,j}^n + \frac{\Delta t}{2} U_t(x_i, y_j, t^n)$$

$$\bar{U}_{i,j}^{n+1} = \frac{1}{4\Delta x \Delta y} \left(\iint_{C_{i+\frac{1}{2},j+\frac{1}{2}}} U_{i+\frac{1}{2},j+\frac{1}{2}}^{n+1} dx dy + \iint_{C_{i-\frac{1}{2},j+\frac{1}{2}}} U_{i-\frac{1}{2},j+\frac{1}{2}}^{n+1} dx dy + \iint_{C_{i+\frac{1}{2},j-\frac{1}{2}}} U_{i+\frac{1}{2},j-\frac{1}{2}}^{n+1} dx dy + \iint_{C_{i-\frac{1}{2},j-\frac{1}{2}}} U_{i-\frac{1}{2},j-\frac{1}{2}}^{n+1} dx dy \right)\quad (27)$$

The discrete derivatives $\dot{U}_{i,j}$ and staggered derivatives $\dot{U}_{i+\frac{1}{2},j+\frac{1}{2}}$ are computed using a limiter function at time t^n :

$$U_{i,j} = MM \left\{ \alpha(U_{i+1,j} - U_{i,j}), \frac{1}{2}(U_{i+1,j} - U_{i-1,j}), \alpha(U_{i,j} - U_{i-1,j}) \right\} (1 \leq \alpha \leq 2) \quad (28)$$

Here, MM is the min-mod limiter function:

$$MM\{a_1, a_2, \dots, a_k, \dots\} = \begin{cases} \min(a_k) & \text{if } a_k > 0 \forall k \\ \max(a_k) & \text{if } a_k < 0 \forall k \\ 0 & \text{otherwise} \end{cases} \quad (29)$$

To prevent numerical instabilities, the time steps are computed according to the Courant criterion:

$$Courant = \frac{1}{2\alpha} (\sqrt{4 + 4\alpha - \alpha^2} - 4) (1 \leq \alpha \leq 4)$$

$$dt = \frac{Courant \cdot \min(\Delta x, \Delta y)}{\rho(A)} \quad (30)$$

Here, $\rho(A)$ is the spectral radius of A .

$$\frac{1}{|\Delta t|} \frac{1}{|I_{i+\frac{1}{2}}|} \int_{t^n}^{t^{n+\frac{1}{2}}} \int_{I_{i+\frac{1}{2}}} (g(U(x, y_{j+1}, t)) - g(U(x, y_j, t))) dx dt$$

$$\approx \frac{1}{|I_{i+\frac{1}{2}}|} \int_{I_{i+\frac{1}{2}}} (g(U(x, y_{j+1}, t^{n+\frac{1}{2}})) - g(U(x, y_j, t^{n+\frac{1}{2}}))) dx$$

$$\approx \frac{1}{2} \{ (g(U_{i,j+1}^{n+\frac{1}{2}}) + g(U_{i+1,j+1}^{n+\frac{1}{2}})) - (g(U_{i+1,j}^{n+\frac{1}{2}}) + g(U_{i,j}^{n+\frac{1}{2}})) \} \quad (24)$$

The staggered form of our central differencing scheme can thus be expressed as:

$$= \bar{U}_{i,j}^n - \frac{\Delta t}{2} f_x(U(x_i, y_j, t^n)) - \frac{\Delta t}{2} g_y(U(x_i, y_j, t^n)) \quad (26)$$

Finally, the staggered form can be transformed into non-staggered form. The non-staggered cell averages $\bar{U}_{i,j}^{n+1}$ using a similar method:

References

- Amos CL, Bergamasco A, Umgiesser G, Cappucci S, Cloutier D, Denat L, Flindt M, Bonardi M, Cristante S (2004) The stability of tidal flats in Venice lagoon — the results of in-situ measurements using two benthic, annular flumes. J Mar Syst 51(1):211–241
- Anandale GW (2006) Scour technology- mechanics and engineering practice. McGraw-Hill, New York
- Bohorquez P, Carling P, Herget J (2015) Dynamic simulation of catastrophic late Pleistocene glacial-lake drainage, Altai Mountains, Central Asia. Int Geol Rev 58(14):1795–1817
- Bread ECP, Dufek J, Roche O (2019) Continuum modeling of pressure- balanced and fluidized granular flows in 2-D: comparison with glass bead experiments and implications for concentrated pyroclastic density currents. Journal of Geophysical Research: Solid Earth 124:5557–5583
- Cao Z (1999) Equilibrium near-bed concentration of suspended sediment. J Hydraul Eng 125(12):1270–1278
- Cao Z, Pender G, Wallis S, Carling P (2004) Computational dam-break hydraulics over erodible sediment bed. J Hydraul Eng 130(7):689–703
- Cao Z, Yue Z, Pender G (2011a) Landslide dam failure and flood hydraulics. Part I: experimental investigation. Nat Hazards 59(2):1003–1019
- Cao Z, Yue Z, Pender G (2011b) Landslide dam failure and flood hydraulics. Part II: coupled mathematical modelling. Nat Hazards 59(2):1021–1045
- Carrick JL (2010) Dam break - outburst flood propagation and transient hydraulics: a geosciences perspective. J Hydrol 380(3–4):338–355
- Casagli N, Ermini L, Rosati G (2003) Determining grain size distribution of the material composing landslide dams in the Northern Apennines: sampling and processing methods. Eng Geol 69:83–97

- Chang DS, Zhang LM (2010) Simulation of the erosion process of landslide dams due to overtopping considering variations in soil erodibility along depth. *Nat Hazards Earth Syst Sci* 10(4):933–946
- Chang DS, Zhang LM, Xu Y, Huang RQ (2011) Field testing of erodibility of two landslide dams triggered by the 12 May Wenchuan earthquake. *Landslides* 8(3):321–332
- Chen SC, Peng SH (2006) Two-dimensional numerical model of two-layer shallow water equations for confluence simulation. *Adv Water Resour* 29(11):1608–1617
- Costa JE, Schuster RL (1988) The formation and failure of natural dams. *Geol Soc Am Bull* 100:1054–1068
- Crosta GB, Calvetti F, Imposimato S, Roddeman D, Frattini P, Agliardi F (2001) Granular flows and numerical modelling of landslides. In: Report of DAMOCLES project, pp 16–36
- Delaney KB, Evans SG (2015) The 2000 Yigong landslide (Tibetan Plateau), rockslide-dammed lake and outburst flood: review, remote sensing analysis, and process modelling. *Geomorphology* 246:377–393
- Denlinger RP, DRH O'C (2009) Simulations of cataclysmic outburst floods from Pleistocene Glacial Lake Missoula. *Geol Soc Am Bull* 122(5–6):678–689
- Fan X, Tang CX, van Westen CJ, Alkema D (2012) Simulating dam-break flood scenarios of the Tangjiaoshan landslide dam induced by the Wenchuan Earthquake. *Nat Hazards Earth Syst Sci* 12(10):3031–3044
- Fraccarollo L, Capart H (2002) Riemann wave description of erosional dam-break flows. *J Fluid Mech* 461:183–228
- Gu DZ (1979) Engineering geological mechanics foundation of rock. Science Press:10–68 (In Chinese)
- Han L, Zhang J, Zhang Y, Ma Q, Alu S, Lang Q (2019) Hazard assessment of earthquake disaster chains based on a Bayesian network model and ArcGIS. *ISPRS Int J Geo Inf* 8.
- Hanson G, Simon A (2001) Erodibility of cohesive steambeds in the loess area of the midwestern USA. *Hydro Process* 15(1):23–28
- Hanson GJ, Cook KR (1997) Development of excess shear stress parameters for circular jet testing. American Society of Agricultural Engineers Paper 972227, ASAE, St. Joseph, MI
- Iverson RM (2012) Elementary theory of bed-sediment entrainment by debris flows and avalanches. *J Geophys Res* 117:F03006
- Jiang GS, Levy D, Lin CT, Osher S, Tadmor E (1999) High-resolution nonoscillatory central schemes with nonstaggered grids for hyperbolic conservation laws. *SIAM J Numer Anal* 35(6):2147–2168
- Jop P, Forterre Y, Pouliquen O (2006) A constitutive law for dense granular flows. *Nature* 441(7094):727–730
- Julian JP, Torres R (2006) Hydraulic erosion of cohesive riverbanks. *Geomorphology* 76(1–2):193–206
- Kurganova A, Tadmor E (2000) New high-resolution central schemes for nonlinear conservation laws and convection–diffusion equations. *J Comput Phys* 160(1):241–282
- Liu W, He SM (2018) Dynamic simulation of a mountain disaster chain: landslides, barrier lakes, and outburst floods. *Nat Hazards* 90(2):757–775
- Liu G, Lu X (2000) Analyses on Yigong huge high velocity landslide in Tibet and the cause of formation of debris flows. In: *Tibet Science and Technology*, pp 15–17 (in Chinese)
- Lu RR, Tang BX, Zhu PY (1999) Debris flows and environment in Tibet. Sichuan University Publishing House, Chengdu, pp 32–68 (in Chinese)
- Lucas A, Mangeney A, Ampuero JP (2014) Frictional velocity-weakening in landslides on earth and on other planetary bodies. *Nat Commun* 5(3417)
- Manning R (1891) On the flow of water in open channels and pipes. *Transactions, Institution of Civil Engineers of Ireland* 20:161–207
- Mehta AJ (1988) Laboratory studies on cohesive sediment deposition and erosion. *Physical Processes in Estuaries*, Springer Berlin Heidelberg, pp 427–445
- MiDi GDR (2004) On dense granular flows. *Eur Phys J E* 14(4):341–365
- Mitchener H, Torfs H (1996) Erosion of mud/sand mixtures. *Coast Eng* 29(1–2):1–25
- Nessimahu H, Tadmor E (1990) Non-oscillatory central differencing for hyperbolic conservation laws. *J Comput Phys* 87(2):408–463
- Ockenden MC, Delo E (1988) Consolidation and erosion of estuarine mud and sand mixtures – an experimental study. HR Wallingford, Report No. SR 149
- Pei R, Ni Z, Meng Z, Zhang B, Liao R (2017) Characteristics of secondary mountain disaster chain in Wenchuan earthquake. *Am J Civil Eng* 5(6):414–417
- Roberts J, Jepsen R, Gotthard D, Lick W (1998) Effects of particle size and bulk density on erosion of quartz particles. *J Hydraul Eng* 124(12):1261–1267
- Savage SB, Hutter K (1989) The motion of a finite mass of granular material down a rough incline. *J Fluid Mech* 199:177–215
- Shang Y, Yang Z, Li L, Liu D, Liao Q, Wang Y (2003) A super-large landslide in Tibet in 2000: background, occurrence, disaster, and origin. *Geomorphology* 54:225–243
- Smerdon ET, Beasley RT (1961) Critical tractive forces in cohesive soils. *Agric Eng* 42(1):26–29
- Sweby PK (1984) High resolution schemes using flux limiters for hyperbolic conservation laws. *SIAM J Numer Anal* 21(5):995–1011
- Takahashi T (1991) Debris flow. Balkema, Rotterdam
- Turzewski M, Huntington K, LeVeque R (2019) The geomorphic impact of outburst floods: integrating observations and numerical simulations of the 2000 Yigong flood, Eastern Himalaya. *J Geophys Res:Earth Surface* 124:1056–1079
- Vanoni VA (1964) Measurements of critical shear stress for entraining fine sediments in a boundary layer (California Institute of Technology)
- Walder JS (2016) Dimensionless erosion laws for cohesive sediment. *J Hydraul Eng* 142(2):1–13
- Wang ZH (2000) The scientist in Beijing predicted the burst of Yigong Lake correctly. *Knowledge of Geography* 7:24–26 (in Chinese)
- Wang Z (2008) A thunder at the beginning of the 21st century – the giant Yigong landslide. *Landslides Eng Slopes* 2:2111–2118
- Xu Q, Fan XM, Huang RQ, Westen CV (2009) Landslide dams triggered by the Wenchuan earthquake, Sichuan Province, south west China. *Bull Eng Geol Environ* 68(3):373–386
- Xu Q, Shang Y, van Asch T, Wang S, Zhang Z, Dong W (2012) Observations from the large, rapid Yigong rock slide–debris avalanche, southeast Tibet. *Can Geotech J* 49(5):589–606
- Yamada M, Kumagai H, Matsushi Y, Matsuzawa T (2013) Dynamic landslide processes revealed by broadband seismic records. *Geophys Res Lett* 40:2998–3002
- Yamada M, Mangeney A, Matsushi Y, Matsuzawa T (2018) Estimation of dynamic friction and movement history of large landslides. *Landslides* 15(10):1963–1974
- Yin YP (2000) Characteristics of Bomi–Yigong huge high speed landslide in Tibet and the research on disaster prevention. *Hydrogeol Eng Geol* 4:8–11 (in Chinese)
- Zhang L, Xia T, He J, Chen C (2019) Erosion-based analysis of breaching of Baige landslide dams on the Jinsha River, China, in 2018. *Landslides* 16(10):1965–1979
- Zhou C (2000) Large scale sand flow with wind in north and heavy rainfall in South China in April 2000. *Weather* 26(7):58–59 (in Chinese)
- Zhou GGD, Cui P, Chen HY, Zhu XH, Tang JB, Sun QC (2012) Experimental study on cascading landslide dam failures by upstream flows. *Landslides* 10(5):633–643
- Zhou GGD, Ng CWW, Sun QC (2013) A new theoretical method for analyzing confined dry granular flows. *Landslides* 11(3):369–384
- Zhou J, Cui P, Hao M (2015a) Comprehensive analyses of the initiation and entrainment processes of the 2000 Yigong catastrophic landslide in Tibet, China. *Landslides* 13(1):39–54
- Zhou GGD, Cui P, Tang JB (2015b) Experimental study on the triggering mechanisms and kinematic properties of large debris flows in Wenjia Gully. *Eng Geol* 194:52–61
- Zhou GGD, Zhou M, Shrestha MS, Song DR, Choi C, Cui KF, Peng M, Shi Z, Zhu X, Chen H (2019) Experimental investigation on the longitudinal evolution of landslide dam breaching and outburst floods. *Geomorphology* 334:29–43
- Zhu P, Wang C, Wang Y (2003) Large-scale landslide-debris avalanche in Tibet, China. Formation of an exceptionally serious outburst flood from a landslide dam in Tibet. *Landslide News* 14–15:23–25

G. G. D. Zhou · P. J. C. Roque · Y. Xie · D. Song · Q. Zou · H. Chen

Key Laboratory of Mountain Hazards and Earth Surface Process/Institute of Mountain Hazards and Environment,
Chinese Academy of Sciences (CAS),
Chengdu, China

G. G. D. Zhou · P. J. C. Roque · Y. Xie (✉) · D. Song · Q. Zou · H. Chen

University of Chinese Academy of Sciences,
Beijing, China
Email: xiyeunxu@imde.ac.cn